Land Surface Temperature Retrieval From Landsat 9 TIRS-2 Data Using Radiance-Based Split-Window Algorithm

Mengmeng Wang [ORCID], Miao Li, Zhengjia Zhang [ORCID], Tian Hu [ORCID], Guojin He [ORCID], Zhaoming Zhang [ORCID], Guizhou Wang [ORCID], Hua Li [ORCID], Junlei Tan [ORCID], and Xiuguo Liu [ORCID]

Abstract—The thermal infrared sensor-2 (TIRS-2) carried on Landsat 9 is the newest thermal infrared (TIR) sensor for the Landsat project and provides two adjacent TIR bands, which greatly benefits the land surface temperature (LST) retrieval at high spatial resolution. In this article, a radiance based split window (RBSW) algorithm for retrieving LST from Landsat 9 TIRS-2 data was proposed. In addition, the split-window covariance-variance ratio (SWCVR) algorithm was improved and applied to Landsat 9 TIRS-2 data for estimating atmospheric water vapor (AWV) that is required for accurate LST retrieval. The performance of the proposed method was assessed using the simulation data and satellite observations. Results reveal that the retrieved LST using the RBSW algorithm has a bias of 0.06 K and root-mean-square error (RMSE) of 0.51 K based on validation with the simulation data. The sensitivity analysis exhibited a LST error of $<$1.75 K using the RBSW algorithm when the uncertainties in input parameters (i.e., AWV, emissivity, and at-sensor radiance) were considered. There is a marginal discrepancy between LST retrievals using the estimated AWV and moderate resolution imaging spectroradiometer AWV, with a difference in bias of -0.14 K and RMSE of 0.22 K, which indicates that the improved SWCVR method can provide an optional means to obtain AWV inputted in LST retrieval. With regard to the validation using the in situ measurements, the retrieved LST from Landsat 9 TIRS-2 data exhibits a bias of 0.44 K and RMSE of 1.98 K, respectively, showing a higher accuracy than the USGS Landsat LST product with bias of 1.21 and RMSE of 2.56 K. In conclusion, the proposed algorithm combining RBSW algorithm and improved SWCVR algorithm for LST retrieval from Landsat 9 has a good accuracy without dependence on external atmospheric data, and it is expected to be a reliable method for LST generation from Landsat 9 TIRS-2 data.

Index Terms—Land surface temperature (LST) retrieval, Landsat 9 thermal infrared sensor-2 (TIRS-2) data, radiance-based split window (RBSW) algorithm, split-window covariance-variance ratio (SWCVR) algorithm.

Mengmeng Wang and Zhengjia Zhang are with the School of Geography and Information Engineering, China University of Geosciences, Wuhan 430074, China, and also with the Artificial Intelligence School, Wuchang University of Technology, Wuhan 430223, China (e-mail: wangmm@cug.edu.cn; zhangzj@cug.edu.cn).

Miao Li and Xiuguo Liu are with the School of Geography and Information Engineering, China University of Geosciences, Wuhan 430074, China (e-mail: 1229806797@qq.com; liuxiuguo@cug.edu.cn).

Tian Hu is with the Remote Sensing and Natural Resources Modeling, Department ERIN, LIST, L-4422 Belvaux, Luxembourg (e-mail: hutian@radi.ac.cn).

Guojin He, Guizhou Wang, and Hua Li are with the Aerospace Information Research Institute, Chinese Academy of Sciences, Beijing 100094, China (e-mail: hegj@radi.ac.cn; wanggz@aircas.ac.cn; lihua@radi.ac.cn).

Zhaoming Zhang is with the Key Laboratory of Earth Observation of Hainan Province, Hainan Aerospace Information Research Institute, Beijing 100094, China (e-mail: zhangzm@radi.ac.cn).

Junlei Tan is with the Northwest Institute of Eco-Environment and Resources, Chinese Academy of Sciences, Lanzhou 73000, China (e-mail: tanjunlei@lzb.ac.cn).

Digital Object Identifier 10.1109/JSTARS.2022.3232621

I. INTRODUCTION

AS AN essential climate variable, land surface temperature (LST) is widely used in surface soil moisture estimation [1], [2], crop evapotranspiration estimation [3], [4], calculation of urban heat island intensity [5], [6], [7], [8] and calculation of surface radiative fluxes [9], [10]. Long-term temporal and spatial distribution of LST is pivotal for the studies of surface energy and water balance [11], [12], carbon cycle in the Earth-atmosphere continuum [13], global climate change [14], [15]. Since its wide use, LST has been scheduled as a high-priority parameter of IGBP [16]. Thermal infrared (TIR) remote sensing (RS) is considered as an effective mean to attain LST due to the direct connection between LST and surface thermal emission [17], [18].

Landsat 9, the latest satellite in the Landsat family, was launched on September 27, 2021, which continues the Landsat data record for fifty years [19]. To the great extent, Landsat 9 is a copy of Landsat 8, carrying two sensors, i.e., an operational land imager-2 and a thermal infrared sensor-2 (TIRS-2) [19]. Similar with Landsat 8 TIRS-1, Landsat 9 TIRS-2 has two TIR bands, i.e., band 10 ranged from 9.8 to 11.8 μm and band 11 ranged from 11 to 13 μm. Some previous studies retrieve LST from Landsat 8 TIRS-1 data using multiple single channel methods [20], [21], [22], [23], [24], [25], [26], [27]. In addition, some scholars have recently tried to use split window (SW) algorithm to retrieve LST from Landsat 8 TIR data after stray light correction and achieved comparable LST retrieval accuracy with single-channel algorithm [26], [27], [28]. Following Landsat 8 TIRS-1, USGS recently released the analysis ready data (ARD) LST product developed from Landsat 9 TIRS-2 data using the operational single-channel method [23]. Landsat 9 TIRS-2 is

an improved version of Landsat 8 TIRS-1 by solving two main issues, i.e., the scene select mirror failure and stray light effect [29]. Two adjacent TIR bands of Landsat 9 TIRS-2 allow for the implementation of SW algorithm to retrieve LST.

The SW method is the most widely used method for LST retrieval based on TIR RS data, which utilizes the difference of atmospheric absorption between two adjacent TIR channels centered at 10–12 μm [30]. Since Price first developed an SW method [31], various SW methods have been proposed for LST retrieval [17], which are grouped into two categories: linear SW method [26], [32], [33], [34], [35], [36] and nonlinear SW method [28], [37], [38], [39], [40], [41]. The linear SW method estimates the LST by linearly combining the brightness temperatures measured by the two adjacent TIR bands; whereas the nonlinear SW method adds a term of the square of the difference between two brightness temperatures into the linear one [17]. Many studies have improved the SW method by modeling the effect of land surface emissivity (LSE), viewing zenith angle (VZA), and atmospheric water vapor (AWV) on LST retrieval and integrating them into the coefficients of SW method [35], [42], [43]. In addition, the two-channel SW method was extended to the three- and four-channel SW method in recent studies, and it was found that the three- and four-channel SW method has better results than the two-channel one [44], [45]. However, the three- and four-channel SW methods are not suitable for Landsat 9 TIRS-2 data with only two thermal bands available. By simplifying radiative transfer equation (RTE) and reserving more of the physical mechanism derived from RTE and Planck function, we proposed the radiance-based split-window (RBSW) algorithm with high accuracy of LST retrieval [46]. As such, this article focuses on adapting the RASW algorithm to Landsat 9 TIRS-2 data.

In the implementation of SW algorithm, AWV is required for describing the atmospheric effect [47]. In general, according to spectral region, the AWV estimation algorithms can be grouped into three categories: near-infrared algorithms; TIR algorithms; and microwave algorithms [48]. Since Landsat 9 has only one near-infrared channel and no microwave channel, only the TIR algorithms can be used to estimate AWV from Landsat 9 data. The split window covariance-variance ratio (SWCVR) algorithm was developed by Sobrino et al. [49] for AWV retrieval from TIR data and optimized by Li et al. [48] by introducing two constraints, and adapted to Landsat 8 TIRS-1 data [47] and VIIRS/S-NPP data [50]. The SWCVR method was developed for AVHRR/ATSR TIR data at ∼1 km spatial scale under the assumption that LSE and atmosphere remain the same over the N neighboring pixels [49]. However, constant LSE over the N neighboring pixels is unreasonable for high resolution TIR data with significant spatial heterogeneity. To deal with this problem, in this article, pixel grouping based on LSE is introduced into the SWCVR method to adapt to Landsat 9 TIRS-2 data for estimating AWV.

This article aims to develop an integrated method based on RBSW and SWCVR algorithms to retrieve LST using Landsat 9 TIRS-2 data. The main characteristic of the proposed method is that it simplifies the RTE and reserves more of the physical mechanism derived from RTE without depending on

any external atmospheric data. To assess the performance of the proposed method, a comprehensive simulation dataset was compiled by using the TIGR atmospheric profiles and ASTER emissivity library. Meanwhile, *in situ* measurements from the surface radiation budget (SURFRAD) network over the contiguous U.S. and the Heihe watershed allied telemetry experimental research (HiWATER) experiment over northwestern China were used to validate all the Landsat 9 LST retrievals available since its launch.

II. METHODOLOGY

A. Radiance Based Split Window Algorithm

Different from the other SW algorithms, the RBSW algorithm uses at-sensor radiance for two adjacent TIR channels as input, instead of at-sensor brightness temperature. First, the black body equivalent-surface emittance is retrieved from two at-sensor radiances using the SW equation, and then LST is estimated from the black body equivalent-surface emittance using the inverse of the Planck function. The RBSW algorithm for retrieving LST from Landsat 9 TIRS-2 can be written as [46]

$$T_s = \frac{c_2 \lambda_{10}^{-1}}{\text{LN}\left(\frac{c_1 \lambda_{10}^{-5}}{B_{10}(T_S)} + 1\right)} \tag{1}$$

with

$$B_{10}\,(T_S) = A_0\,L_{10} + A_1 L_{11} + A_2 \tag{2}$$

where T_s represents the LST; LN represents natural logarithm function; $B_{10}(T_S)$ represents the blackbody radiance with a temperature of LST; L_{10} and L_{11} represent the at-sensor radiances for bands 10 and 11; $c_1 = 1.19104 \times 10^8$ Wμm4m^{-2}sr^{-1} and $c_2 = 1.43877 \times 10^4$ μmK; λ_{10} is the effective wavelength for band 10 (10.8372 μm); A_0, A_1 and A_2 are intermediate variables of RBSW algorithm and can be calculated from

$$A_0 = \frac{D_{11}}{C_{10}D_{11} - C_{11}D_{10}} \tag{3}$$

$$A_1 = \frac{-D_{10}}{k\,(C_{10}D_{11} - C_{11}D_{10})} \tag{4}$$

$$A_2 = \frac{bD_{10}\,(C_{11} + D_{11})}{k\,(C_{10}D_{11} - C_{11}D_{10})} \tag{5}$$

with

$$C_{10/11} = \varepsilon_{10/11}\,\tau_{10/11} \tag{6}$$

$$D_{10/11} = \left(1 - \tau_{10/11}\right)\left[\left(1 - \varepsilon_{10/11}\right)\tau_{10/11}\varphi_{10/11} + 1\right] \tag{7}$$

where $\varepsilon_{10/11}$ is the LSE for band 10 or 11; k and b are the radiative parameters used for radiance conversion between two bands based on Planck's function; and $\tau_{10/11}$ and $\varphi_{10/11}$ are the atmospheric parameters for band 10 or 11, respectively. k and b can be calculated from L_{10} and the effective wavelength for bands 10 and 11 using the following formulas:

$$k = \frac{c_1^2 \lambda_{10}^{-4} \lambda_{11}^{-6} \left(c_1 \lambda_{10}^{-5} L_{10}^{-1} + 1\right)^{\left(\lambda_{10}\lambda_{11}^{-1} - 1\right)}}{\left[\left(c_1 \lambda_{10}^{-5} L_{10}^{-1} + 1\right)^{\left(\lambda_{10}\lambda_{11}^{-1}\right)} - 1\right]^2 L_{10}^2} \tag{8}$$

TABLE I
COEFFICIENTS a_k ($k = 0, 1, \ldots 3$) OF RBSW ALGORITHM FOR LANDSAT 9
TIRS BANDS 10 AND 11

	a_0	a_1	a_2	a_3
Landsat 9 TIRS band 10	-0.0523	0.9495	1.4073	1.1641
Landsat 9 TIRS band 11	-0.0531	0.8315	0.6079	0.4856

$$b = \frac{c_1 \lambda_{11}^{-5}}{\left(c_1 \lambda_{10}^{-5} L_{10}^{-1} + 1\right)^{\left(\lambda_{10} \lambda_{11}^{-1}\right)} - 1} - k L_{10} \qquad (9)$$

where λ_{11} is the effective wavelength for band 11 (12.0253 μm). Since the maximum VZA of Landsat 9 TIRS-2 is about 7.5°, the effect of VZA on the RTE is insignificant [36]. Thus, the formulas for calculating $\tau_{10/11}$ and $\varphi_{10/11}$ can be rewritten as

$$\tau_{10/11} = a_0 w + a_1 \qquad (10)$$

$$\varphi_{10/11} = a_2 LN(w) + a_3 \qquad (11)$$

where w is the AWV; a_k ($k = 0, 1, \ldots 3$) are coefficients of RBSW algorithm for Landsat 9 TIRS-2 data and can be obtained from a simulation dataset.

The simulation dataset was constructed by atmospheric radiative transfer code MODTRAN 5.2 with input of surface characteristics and atmospheric conditions, and spectrally resampled using the spectral response function of Landsat 9 TIRS-2 sensor. 1393 clear-sky atmospheric profiles were selected from TIGR2000 dataset, in which profiles with the relative humidity greater than 90% in any layer were considered as cloudy, and inputted into MODTRAN as the atmospheric conditions. A total of 81 selected ASTER emissivity samples were used as surface characteristics, including 13 rock samples, 54 soil samples, 4 man-made samples, 4 vegetation samples and 6 water-ice-snow samples. In addition, eight grades of LST were set based on the bottom air temperature (T_b), including $T_b - 10$ K, $T_b - 5$ K, T_b, $T_b + 5$ K, $T_b + 10$ K, $T_b + 15$ K, $T_b + 20$ K, $T_b + 25$ K [25]. In total 902 664 simulation data were obtained (1393 atmospheric profiles× 8 LSTs × 81 emissivities) and divided into two groups. Two thirds of simulation data were used for fitting RBSW algorithm (named as SD1), and remaining third were employed for validating the RBSW algorithm (named as SD2). The coefficients of RBSW algorithm for Landsat 9 TIRS-2 data were calculated by global fitting the RBSW algorithm based on the SD1, as given in Table I and Fig. 1.

B. Estimation of Land Surface Emissivity

With the pronounced advantage of its simplicity, the normalized difference vegetation index thresholds Method (NDVI$^{\text{THM}}$) has been applied to various VNIR and TIR instruments, such as Landsat 4/5/7/8 [51]. The soil component emissivity calculated from ASTER GED LSE data can be used to further improve the Landsat LSE estimation using NDVI$^{\text{THM}}$ [52]. Introducing ASTER GED LSE data into NDVI$^{\text{THM}}$, the LSE estimation for Landsat 9 TIRS-2 bands 10 and 11 involves three steps. First, the bare soil emissivities for the ASTER TIR bands 13 and 14 are obtained by removing the vegetation component from the ASTER emissivity using the fractional vegetation cover (FVC)
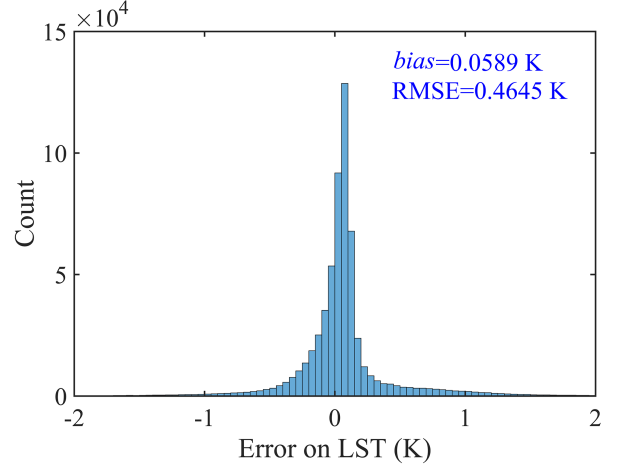

Fig. 1. Histogram of the error on LST of the fitting RBSW algorithm using the simulation data.

[23].

$$\varepsilon_{A13/A14, \text{ bare}} = \frac{\varepsilon_{A13/A14} - \varepsilon_{A13/A14, \text{ veg}} f_{\text{ASTER, veg}}}{1 - f_{A13/A14, \text{ veg}}} \qquad (12)$$

where $\varepsilon_{A13/A14}$ represents the LSE for ASTER band 13 or 14 from ASTER GEDV3 dataset, $\varepsilon_{A13/A14, \text{ bare}}$ represents the emissivity of bare soil for ASTER band 13 or 14, $\varepsilon_{A13/A14, \text{ veg}}$ represent the pure vegetation emissivity for ASTER band 13 or 14, $f_{\text{ASTER, veg}}$ represents ASTER FVC. And then, the estimated emissivities of bare soil for ASTER bands 13 and 14 are spectrally adjusted to that for Landsat 9 TIRS-2 bands 10 and 11 using regressed linear equations as follows [53]:

$$\varepsilon_{10/11, \text{ bare}} = b_0 \varepsilon_{A13, \text{ bare}} + b_1 \varepsilon_{A14, \text{ bare}} + b_2 \qquad (13)$$

where $\varepsilon_{10/11, \text{ bare}}$ represents the emissivity of bare soil for Landsat 9 TIRS-2 band 10 or 11, b_k ($k = 0, 1, 2$) represent the coefficients of the regression equation. Finally, the LSE for Landsat 9 TIRS-2 bands 10 and 11 is estimated by adding vegetation emissivity information to the Landsat bare soil emissivity using the Landsat FVC as follows [51]:

$$\varepsilon_{10/11} = f_{\text{Landsat, veg}} \cdot \varepsilon_{L10/11, \text{ veg}} + (1 - f_{\text{Landsat, veg}}) \cdot \varepsilon_{10/11, \text{ bare}} \qquad (14)$$

where $\varepsilon_{10/11}$ represents the LSE for Landsat 9 band 10 or 11, $\varepsilon_{10/11, \text{ veg}}$ represents the emissivity of pure vegetation for Landsat 9 band 10 or 11, $f_{\text{Landsat, veg}}$ represents Landsat FVC. Landsat and ASTER FVC can be calculated as follows [54]:

$$f_{\text{ASTER/Landsat, veg}} = \left(\frac{\text{NDVI}_{\text{ASTER/Landsat}} - \text{NDVI}_{\text{ASTER/Landsat, bare}}}{\text{NDVI}_{\text{ASTER/Landsat, veg}} - \text{NDVI}_{\text{ASTER/Landsat, bare}}}\right)^2 \qquad (15)$$

where $\text{NDVI}_{\text{ASTER/Landsat}}$ represents the ASTER/Landsat NDVI, $\text{NDVI}_{\text{ASTER/Landsat, veg}}$ and $\text{NDVI}_{\text{ASTER/Landsat, bare}}$ represent the ASTER/Landsat NDVI for pure vegetation and bare soil, with value of 0.86 and 0.2, respectively [55]. Based on the similar method, replacing NDVI with normalized

TABLE II
COEFFICIENTS b_k ($k = 0, 1, 2$) FOR LANDSAT 9 TIRS-2 BANDS 10 AND 11

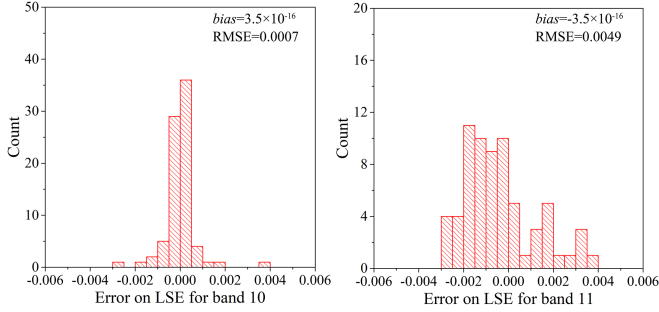|	b_0	b_1	b_2
Landsat 9 TIRS band 10	0.7109	0.2972	-0.0075
Landsat 9 TIRS band 11	0.0545	0.4579	0.4799

Fig. 2. Histograms of error in LSE for band 10 (left) and for band 11 (right) using regressed linear equations.

TABLE III
EMISSIVITIES OF PURE VEGETATION, SNOW AND WATER FOR LANDSAT 9 TIRS-2 BANDS 10 AND 11, AND ASTER BANDS 13 AND 14

	Emissivity for pure vegetation	Emissivity for snow	Emissivity for water
L9 B10	0.9816	0.9910	0.9907
L9 B11	0.9843	0.9773	0.9854
ASTER B13	0.9813	0.9931	0.9905
ASTER B14	0.9827	0.9848	0.9904

difference snow index, the impact of snow cover on the emissivity estimation is adjusted.

A set of emissivity samples from ASTER spectral library was employed to fit the (13) and calculate emissivities for pure vegetation, snow and water for Landsat 9 TIRS-2 bands 10 and 11, and ASTER bands 13 and 14. The spectral emissivity was converted to the band-effective emissivity by spectral resampling with spectral response function of Landsat 9 TIRS-2 and ASTER TIR bands. The regression coefficients b_k ($k = 0, 1, 2$) for Landsat 9 TIRS-2 bands 10 and 11 were calculated by fitting the (13) based on 71 samples, including 13 rock samples, 54 soil samples and 4 man-made samples, as given in Table II and Fig. 2. Emissivities of pure vegetation, snow and water were calculated by averaging emissivities of three vegetation samples, three snow samples, and two water samples, respectively, and the results for Landsat 9 TIRS-2 bands 10 and 11, and ASTER bands 13 and 14 are given in Table III.

C. Calculation of Atmospheric Water Vapor Content

Assuming that LSE and atmosphere remain unchanged, or the influences of their spatial variations are less than instrument noise effect over the N neighboring pixels, the SWCVR algorithm for retrieving AWV from Landsat 9 TIRS-2 data can be written as (Li et al. 2003 and Sobrino et al. 1994)

$$w = c_0 \left(\frac{\tau_{11}}{\tau_{10}} \right) + c_1 \quad (16)$$

with

$$\frac{\tau_{11}}{\tau_{10}} = \frac{\varepsilon_{10}}{\varepsilon_{11}} \cdot \frac{\sum_{k=1}^{N} (T_{10,k} - T_{10}^*)(T_{11,k} - T_{11}^*)}{\sum_{k=1}^{N} (T_{10,k} - T_{10}^*)^2} \quad (17)$$

$$r^2 = \frac{\left(\sum_{k=1}^{N} (T_{10,k} - T_{10}^*)(T_{11,k} - T_{11}^*) \right)^2}{\sum_{k=1}^{N} (T_{10,k} - T_{10}^*)^2 \sum_{k=1}^{N} (T_{11,k} - T_{11}^*)^2} \quad (18)$$

where w represents AWV; τ_{10} and τ_{11} represent transmittance of TIRS-2 bands 10 and 11; c_0 and c_1 represent the coefficients of AWV model; k represents pixel k; $T_{10,k}$ and $T_{11,k}$ represent brightness temperature of TIRS-2 bands 10 and 11 for pixel k; T_{10}^* and T_{11}^* represent the mean brightness temperature of Landsat 9 TIRS-2 bands 10 and 11 over N pixels, respectively; r^2 represents the correlation coefficient between two brightness temperatures (i.e., $T_{10,k}$ and $T_{11,k}$) for the N neighboring pixels, which is used to test whether the assumptions made for (17) are valid. According to the work of Li et al. [48], a reliable result requires a r^2 value no less than 0.95. The coefficients c_0 and c_1 were calculated by fit the (16) using the SD1 (see Section II-A), as shown in Fig. 3.

The SWCVR method is developed for TIR data at coarse spatial resolution (e.g., AVHRR/ATSR TIR data with ~1 km spatial resolution), when applied to Landsat 9 TIRS-2 at a spatial resolution of 0.1 km, it has some limitations and needs to be improved. There is an important assumption that LSE over the N neighboring pixels remains constant in SWCVR method. However, this assumption is unreasonable for high resolution TIR data with significant spatial heterogeneity. In this article, therefore, pixel grouping based on the LSE ratio is introduced to adapt SWCVR method to Landsat 9 TIRS-2 data. The N neighboring pixels are grouped with equal-interval based on the maximum and maximum emissivity ration ($\frac{\varepsilon_{10}}{\varepsilon_{11}}$) of the whole image and the number of groups (*M*). The comprehensive AWV (*w*) for N neighboring pixels is calculated from the AWV and pixel number of the effective group with r^2 of larger than 0.95 using the weighted sum method as follows:

$$w = \frac{\sum_{i=1}^{i=M} N_i w_i}{\sum_{i=1}^{i=M} N_i} \quad (19)$$

where w_i represents the AWV for group i calculated using the (16), N_i represents the valid pixel number for group i.

In the original SWCVR method, the emissivity ratio ($\frac{\varepsilon_{10}}{\varepsilon_{11}}$) is taken as 1 at a kilometer scale considering the pixel is mixed by different types of surfaces. However, the variation of emissivity ratio ($\frac{\varepsilon_{10}}{\varepsilon_{11}}$) for high resolution TIR data is larger than that of coarse spatial resolution. In this article, the mean emissivity ratio ($\frac{\varepsilon_{10}}{\varepsilon_{11}}$) for each group is estimated and used in (17) to improve the calculation of the transmittance ratio.
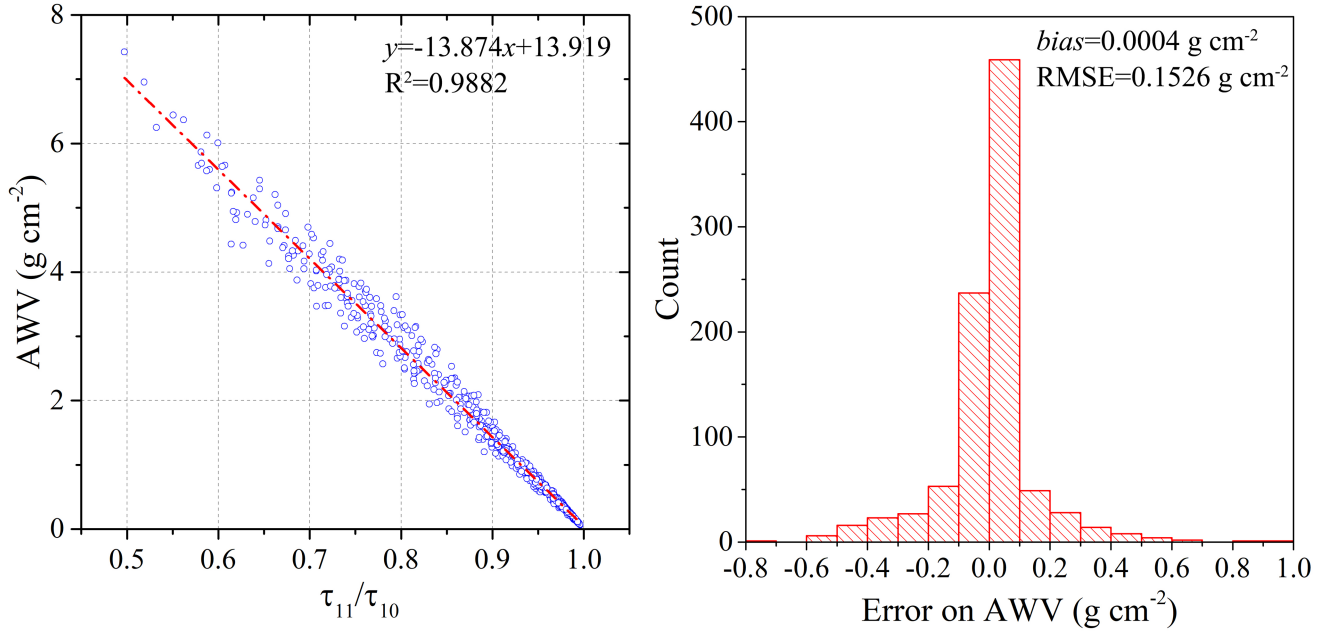
Fig. 3. Relationship between AWV and the transmittance ratio of bands 11 and 10 (right) and the histogram of error on AWV based on the linear regression relationship (left).

TABLE IV
DETAILS OF THE HiWATER AND SURFRAD SITES

Name	Country	Latitude	Longitude
Amity_Univ_Gurgaon	India	28.317N	76.916E
Apulian_Tavoliere	Italy	41.461N	15.502E
Aubiere_LAMP	France	45.761N	3.111E
Beijing	China	39.977N	116.381E
Beijing_PKU	China	39.992N	116.310E
Beijing-CAMS	China	39.933N	116.317E
Cairo_EMA_2	Egypt	30.081N	31.290E
Chachoengsao	Thailand	13.500N	101.450E
Chiang_Dao	Thailand	19.455N	98.961E
Dakar_Belair	Senegal	14.702N	17.426W
Gangneung_WNU	South_Korea	37.771N	128.867E
Doi_Ang_Khang	Thailand	19.932N	99.045E

D. Validation of AWV Using in situ Data

The AERONET program provides long-term, continuous, global observations of spectral aerosol optical depth, precipitable water, and other related parameters to support aerosol research and characterization, validation of satellite retrievals [47]. The AWV was estimated using the observed data in the water absorption band (approximately 940 nm) [56], [57]. A total of 12 AERONET stations (see Table IV) were chosen for the validation of AWV retrieved using the SWCVR and the improved SWCVR methods.

In order to compare with in situ AWV, the retrieved AWV are spatially matched with each AERONET site based on the

longitude and latitude of the site. The in situ AWV for the transit time of Landsat 9 satellite is calculated by linearly interpolating two in situ measurements temporally closest to the transit time. Then, a pair of retrieved and in situ AWVs can be generated through spatially and temporally matching.

E. Validation of LST Using in situ Data

The continuous and high-quality surface radiation budget and meteorological measurements taken from SURFRAD and HiWATER networks can promote the RS retrieval validation and climatology studies [58], [59], [60], [61]. The temporal resolution of longwave radiation measurements at SURFRAD and HiWATER sites is 1 to 3 min. Four SURFRAD sites and two HiWATER sites have been employed to validate the retrieved LST from Landsat 9 TIRS-2 data, see Table V and Fig. 4. in situ LST T_s was estimated from measured broadband upwelling and downwelling longwave radiation measured (i.e., R_g and R_d) from SURFRAD and HiWATER sites based on the Stefan-Boltzmann law [21], [62]:

$$T_s = \left[\frac{R_g - (1 - \varepsilon_b) R_d}{\varepsilon_b} \right]^{1/4} \quad (20)$$

where ε_b represents broadband emissivity and can be calculated from ASTER narrowband emissivity using the following regression equation [63]:

$$\varepsilon_b = 0.197 + 0.025\varepsilon_{A10} + 0.057\varepsilon_{A11} + 0.237\varepsilon_{A12}$$
$$+ 0.333\varepsilon_{A13} + 0.146\varepsilon_{A14} \quad (21)$$

where ε_{A10} to ε_{A14} represent the LSE for ASTER bands 10 to 14. The retrieved LST and in situ LST were spatially and temporally matched to generate LST pairs, similar as validation of AWV.

TABLE V
DETAILS OF THE HIWATER AND SURFRAD SITES

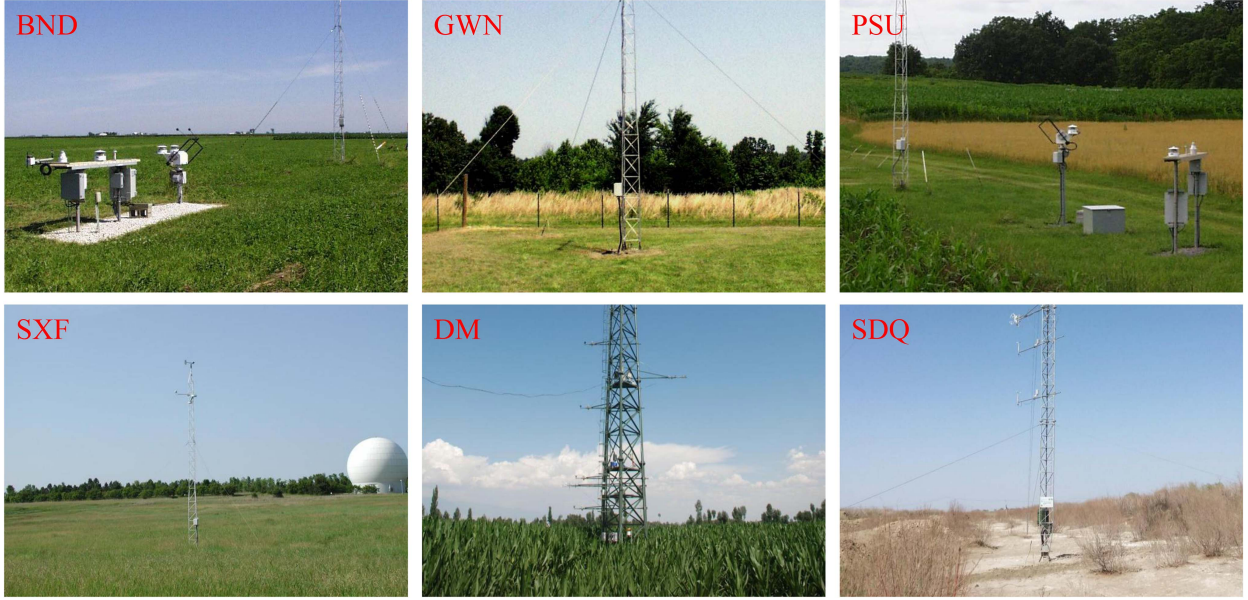| Station name	Station code	Latitude	Longitude	Altitude	Land cover
Bondville, IL.	BND	40.0516°N	88.3733°W	230 m	Cropland
Fort Peck, MT.	FPK	48.3080°N	105.1018°W	634 m	Grassland
Goodwin Creek, MS.	GCM	34.2547°N	89.8729°W	98 m	Grassland
Sioux Falls, SD.	SXF	43.7343°N	96.6233°W	473 m	Grassland
Daman	DM	38.8555° N	100.3722° E	1556 m	Cropland
Sidaoqiao	SDQ	42.0012° N	101.1374° E	873 m	Shrub-lands

Fig. 4 Photographs of the four SURFRAD sites (i.e., BND, GWN, PSU, and SXF) and two ARM sites (i.e., DM and SDQ).

TABLE VI
BIAS AND RMSE BETWEEN THE RETRIEVED AND SIMULATED LSTS AT DIFFERENT AWV RANGES (G CM^{-2})

w (g cm^{-2})	0~1	1~2	2~3	3~4	4~5	5~6	6~7	Total
Number	188568	35640	33696	21384	11664	8424	1296	300672
bias (K)	0.04	-0.08	0.02	0.21	0.54	0.14	0.21	0.06
RMSE (K)	0.10	0.28	0.44	0.85	1.11	1.85	2.37	0.51

III. RESULTS

A. Validation of the RBSW Algorithm Using Simulation Data

The performance of the RBSW algorithm for Landsat 9 TIRS-2 data was assessed using SD2 (see Section II-A). As shown in Fig. 5, LST errors concentrate around zero under low AWV, and are more scattered with increasing AWV. The main reason is the larger influence of atmosphere on LST retrieval from satellite data with the AWV increasing. The correction to atmospheric effect for LST retrieval has greater uncertainty within higher AWV conditions. As given in Table VI, the bias of RBSW algorithm is close to zero except for AWV range from 4.0 to 5.0 g cm^{-2}. The RMSE of RBSW algorithm increases with increasing of AWV, and the RMSE increases from 0.10 to 2.37 K when the AWV is lower than 7 g cm^{-2}. The RMSE is less than 1 K when AWV is lower than 5.0 g cm^{-2} and less than 2.50 K

when AWV is lower than 7.0 g cm^{-2}. The total bias and total RMSE of RBSW algorithm for whole AWV range are 0.06 and 0.51 K, respectively. Table VII gives bias and RMSE between the retrieved and simulated LSTs for different types of land cover. The RMSE of RBSW algorithm for different land cover types are close, and the RMSE difference is less than 0.15 K. There is a weak growth trend of RMSE from man-made (0.42 K), soil (0.47 K), rock (0.53 K), vegetation (0.56 K) to water-snow-ice (0.59 K). This indicated that the RMSE slightly increases with the increasing of LSE based on the simulation data validation in which there are no error in input parameter.

B. Sensitivity Analysis of RBSW Algorithm

The sensitivity of RBSW algorithm to LSE, at-sensor radiance and AWV was analyzed considering different AWV and

TABLE VII
BIAS AND RMSE BETWEEN THE RETRIEVED AND SIMULATED LSTs FOR DIFFERENT TYPES OF LAND COVER

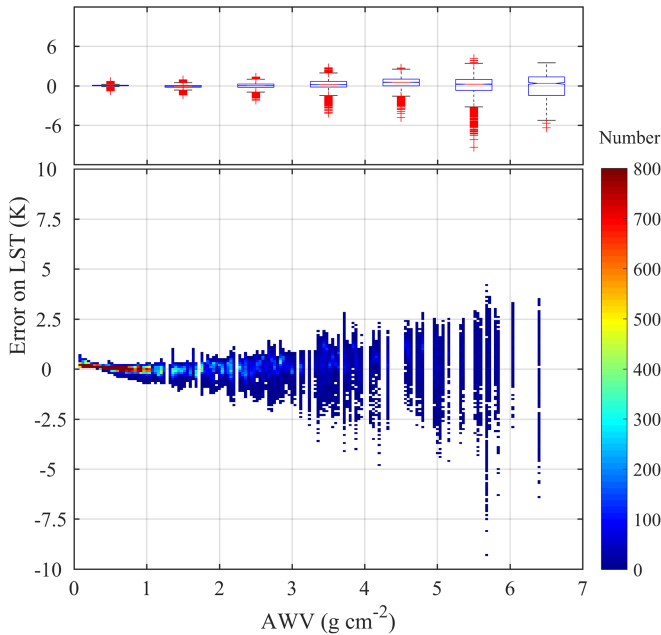| Type	Man-made	Soil	Rock	Vegetation	Water-snow-ice
Number	14848	300672	51968	11136	22272
bias	0.06	0.08	-0.02	0.14	0.09
RMSE	0.42	0.47	0.53	0.56	0.59

Fig. 5. Box plot (top) and density scatter plot (bottom) of the difference between the retrieved LST for RBSW algorithm and simulated LST.

LSE conditions, as shown in Fig. 6. Fig. 6(a)–(c) represents the possible error of estimated LST using RBSW algorithm aroused by the probable LSE error. The RBSW algorithm is more sensitive to the error in ε_{10} than to the error in ε_{11} and the same errors in both ε_{10} and ε_{11}. Such as, at AWV of 2 g cm^{-2}, an ε_{10} error of 0.01 arouses a LST error of 0.91 K, whereas an ε_{11} error of 0.01 arouses a LST error of 0.57 K, and the same ε_{10} and ε_{11} error of 0.01 arouses a LST error of 0.37 K. This is because that the LST is directly calculated from $B_{10}(T_s)$ and ε_{10} using the (1) of RBSW algorithm. Fig. 6(d)–(f) represents the possible error of estimated LST using RBSW algorithm aroused by the probable at-sensor radiance error. The LST estimation error aroused by the at-sensor radiance error in single band increases with the AWV, whereas the LST estimation error aroused by the at-sensor radiance error in both bands 10 and 11 marginally changes with the AWV. The RBSW algorithm is more sensitive to the at-sensor radiance error in a single channel than to the same error on L_{10} and L_{11}. For example, at AWV of 2 g cm^{-2}, an L_{10} error of 0.04 Wm^{-2}sr$^{-1}\mu$m^{-1} (i.e., NEΔT of 0.28 K at 300 K) causes a LST error of 0.67 K, an L_{11} error of 0.04 Wm^{-2}sr$^{-1}\mu$m^{-1} causes a LST error of 0.46 K, whereas the same L_{10} and L_{11} error of 0.04 Wm^{-2}sr$^{-1}\mu$m^{-1} arouses a LST error of 0.21 K. Fig. 6(g) and (i) represents the possible error of estimated LST using RBSW algorithm aroused by the probable AWV error under low LSE (i.e., $\varepsilon_{10} = 0.949$ and $\varepsilon_{11} = 0.955$),

moderate LSE (i.e., $\varepsilon_{10} = 0.961$ and $\varepsilon_{11} = 0.967$) and high LSE (i.e., $\varepsilon_{10} = 0.981$ and $\varepsilon_{11} = 0.987$) conditions. The error in LST estimation aroused by the AWV error increases with the AWV under low and moderate LSE, whereas the error in LST estimation aroused by the AWV error marginally changes with the AWV under high LSE. The sensitivity of RBSW algorithm to the AWV decrease with the increasing of LSE. Such as, at AWV of 2 g cm^{-2}, an AWV error of 0.6 g cm^{-2} leads to a LST error of 0.43 K for low LSE, 0.26 K for moderate LSE and 0.01 K for high LSE. When the errors of 0.04 Wm^{-2}sr$^{-1}\mu$m^{-1} in L_{10}, 0.01 in ε_{10}, 0.6 g cm^{-2} in AWV, the total errors in LST estimation are 1.10 K for low LSE and low AWV (i.e., 0.5 g cm^{-2}), 1.74 K for low LSE and high w (i.e., 4.5 g cm^{-2}), 1.10 K for high LSE and low w, and 1.53 K for high LSE and high w, respectively.

C. Application of the RBSW Algorithm for Landsat 9 TIRS-2 Data

A Landsat 9 image acquired over southeastern Australia on 13 February 2022 was employed to estimate LSE, AWV, and LST, as shown in Fig. 7. Fig. 7(a) and (b) shows that the LSE of bands 10 and 11 mainly range from 0.96 to 0.99. The vegetation has a higher LSE, whereas the bare land has a lower LSE. The LSE of band 10 is generally lower than that of band 11, which is in agreement with the statistic from LSE spectral library.

In order to obtain the optimal AWV estimation, the AWV results were estimated using different window size and the number of groups and compared with the moderate resolution imaging spectroradiometer (MODIS) AWV. As shown in Fig. 8, the RMSE between MODIS AWV and the retrieved AWV using the improved SWCVR decreases with the increase of window size. There is a sharp decline of RMSE with the window size from 20 to 60, and the RMSE tend to be stable after window size of 80. The RMSE increases with increase of group number when the window size is less than 40; whereas it decreases with increase of group number when the window size is larger than 40. Therefore, the window size is set to 100 to extract the N (100×100) neighboring pixels, and the number of group (M) is set to 3. Fig. 7(c) showed the map of AWV estimated using the improved SWCVR with window size of 100 and group number of 3. The AWV retrieved from Landsat 9 TIRS-2 data are between 1.4 and 2.8 g cm^{-2}. The retrieved AWV has a similar spatial distribution with the MODIS AWV [see Fig. 7(d)], like the AWV over south is larger than that of north. Fig. 9(a) showed the bias and RMSE between MODIS AWV and the retrieved AWV are −0.27 and 0.40 g cm^{-2}, respectively.

Fig. 7(e) shows the map of LST retrieved using RBSW algorithm with input of the retrieved AWV and LSE. The retrieved LST mainly range from 300 and 320 K over the study area.
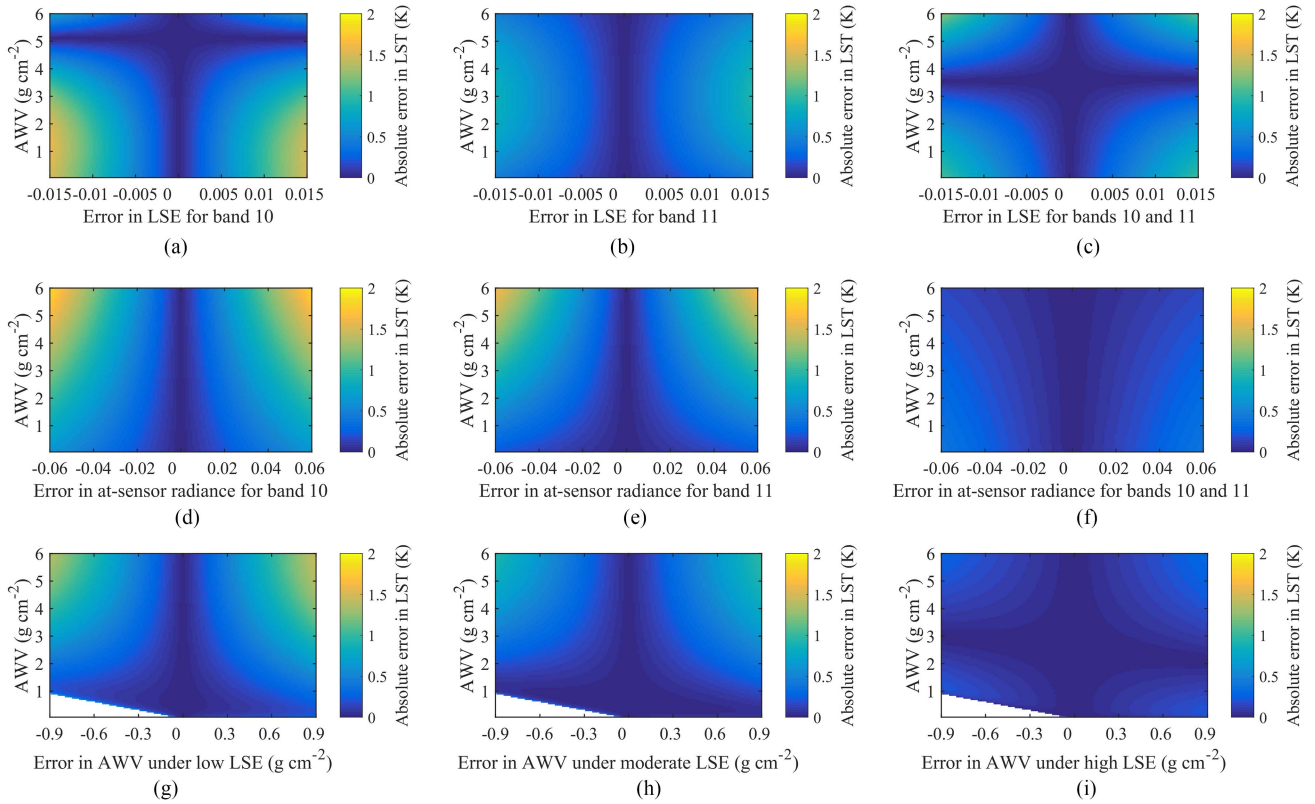
Fig. 6. LST estimation error aroused by the possible LSE error (a, b, and c), at-sensor radiance error (c, d, and f) under different AWV, and LST estimation error aroused by the possible AWV error for low LSE (g), moderate LSE (h) and high LSE (i) conditions under different AWV.

The retrieved LST shows a similar spatial distribution with USGS LST [see Fig. 7(f)], but it is lower than that of USGS LST, especially for high LST region. As shown in Fig. 9(b), the bias (RMSE) between the retrieved LST with input of retrieved AWV and the retrieved LST with input of MODIS AWV are -0.14 K (0.22 K), indicating that the LST retrieval with input of AWV estimated using the improved SWCVR method and MODIS AWV give quite close results. Therefore, the improved SWCVR method can provide an optional means to obtain AWV for LST retrieval from Landsat 9 TIRS-2 data, especial for the region with no overlap between MODIS data and Landsat 9 data. Fig. 9(c) and (d) shows that the bias and RMSE between the retrieved and USGS LSTs are around -1.9 and 2.1 K, respectively. In the following, the in situ LST data was employed to validate the retrieved and USGS LSTs.

D. Evaluation of AWV and LST Retrievals Using in situ Measurements

The evaluation of AWV retrieval from Landsat 9 TIR-2 data based on the SWCVR and the improved SWCVR methods were performed using the in situ AWV measurements from AERONET stations. The acquired date of Landsat 9 data is between November 2021 and November 2022. As shown in Fig. 10, the in situ AWV ranges from 0 to 6 g cm^{-2}. Most of points which are distributed around the 1:1 line present a good accuracy, whereas the less points below the 1:1 line indicate an underestimation of AWV. At the AWV range between 0 and

3 g cm^{-2}, the bias (RMSE) is -0.06 g cm^{-2} (0.48 g cm^{-2}) for SWCVR method and -0.03 g cm^{-2} (0.47 g cm^{-2}) for the improved SWCVR method, respectively, showing a close performance between SWCVR and the improved SWCVR methods. At the AWV range between 3 and 6 g cm^{-2}, the bias (RMSE) is -0.70 g cm^{-2} (1.20 g cm^{-2}) for SWCVR method and -0.59 g cm^{-2} (1.07 g cm^{-2}) for the improved SWCVR method, respectively, indicating the accuracy of the improved SWCVR method is better than SWCVR method. Validation using 173 in situ measurements from 12 AERONET stations shows that the total bias (RMSE) is -0.19 g cm^{-2} (0.69 g cm^{-2}) for SWCVR method and -0.15 g cm^{-2} (0.64 g cm^{-2}) for the improved SWCVR method, respectively.

The evaluation of retrieved LST using RBSW algorithm and USGS LST were performed using in situ LST measurements from HiWATER and SURFRAD networks. The number of Landsat-in situ LST pairs is 58 at SURFRAD sites and 40 at HiWATER sites, in total 98 clear-sky pairs of Landsat and in situ LSTs. As shown in Fig. 11, the in situ LST are between 260 K and 320 K, and has a high relevant correlation with retrieved LST using the proposed method and USGS LST. The bias (RMSE) at SURFRAD sites is 0.57 K (1.73 K) for the proposed method and 0.99 K (2.40 K) for USGS LST, respectively. The bias (RMSE) at HiWATER sites is 0.26 K (2.27 K) for the proposed method and 1.51 K (2.76 K) for USGS LST, respectively. Validation using in situ data shows that the proposed method achieves a good accuracy (with bias of 0.44 K and RMSE of 1.98 K) and is superior than USGS LST (with bias of 1.21 K and RMSE
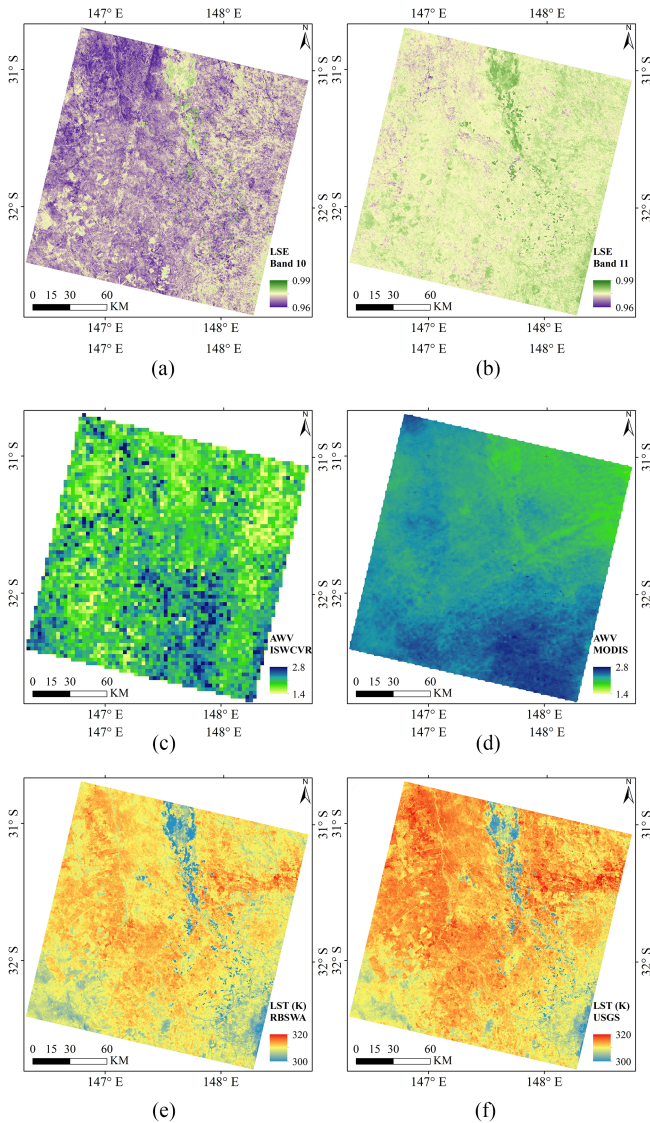
Fig. 7. (a) Map of the LSE for Landsat 9 TIRS-2 bands 10. (b) Map of the LSE for Landsat 9 TIRS-2 band 11. (c) Map of the AWV estimated using the improved SWCVR method. (d) Map of the AWV from MODIS MOD05 product. (e) Map of LST retrieved using the proposed method. (f) Map of the LST from USGS ARD product. Landsat 9 and MODIS data were acquired over Southeastern Australia on 13 February 2022.

of 2.56 K) based on 98 in situ LST data from HiWATER and SURFRAD networks.

IV. DISCUSSION

A. AWV Retrieval From Landsat 9 TIR-2 Data

This article proposed an improved SWCVR method for retrieving AWV from Landsat 9 TIRS-2 data, which relieves the LST retrieval from Landsat TIR data from its dependence on atmospheric auxiliary data. For the previous missions of the Landsat series, different atmospheric auxiliary data have been used for LST retrieval, including meteorological observations, MODIS atmospheric products [64] and reanalysis data [24]. Meteorological data is site-based measurement, which limits its application at large scales, especially for regions where ground
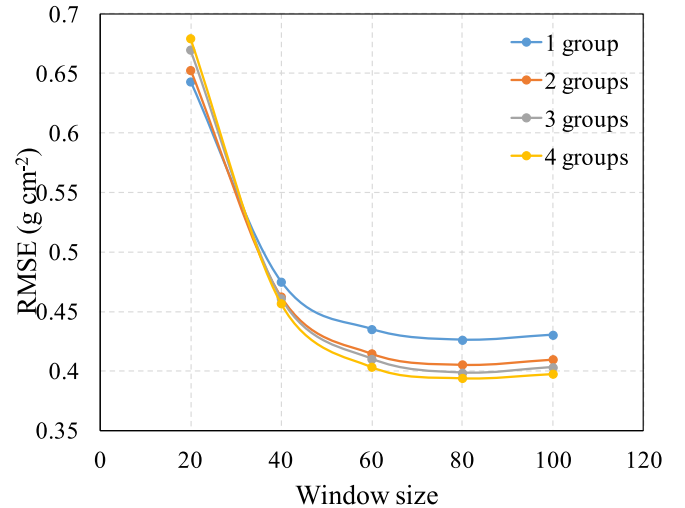

Fig. 8. RMSE between MODIS AWV and the retrieved AWV using the improved SWCVR with different window size and group number.
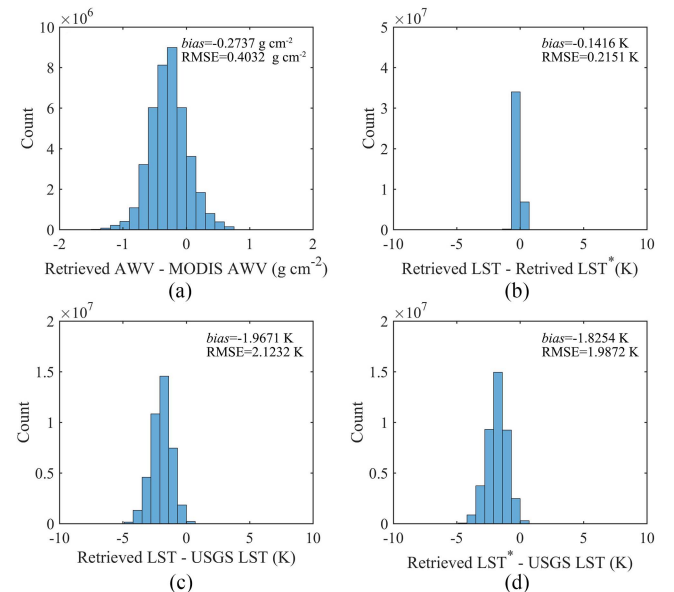

Fig. 9. (a) Histograms of difference between MODIS AWV and the retrieved AWV using the improved SWCVR with window size of 100 and group number of 3 and (b)–(d) between USGS and the retrieved LSTs. Retrieved LST represent LST retrieved using RBSW algorithm with input of the retrieved AWV; Retrieved LST* represent LST retrieved using RBSW algorithm with input of the MODIS AWV.

stations are sparsely distributed [64]. In many regions, the Landsat image cannot be fully covered by the corresponding MODIS image, even no overlap between them [65]. Compared with Landsat TIR data, reanalysis atmospheric data normally have very coarse spatial resolutions, which may cause uncertainties in LST retrieval [55]. The AWV estimation from Landsat 9 TIRS-2 itself using the improved SWCVR method can greatly improve the practicability of LST retrieval.

The accuracy of original SWCVR method increases with the window size and decreases with the number of land cover types (i.e., the LSE types) involved in the window [47]. In general, the number of land cover types included in the window increases
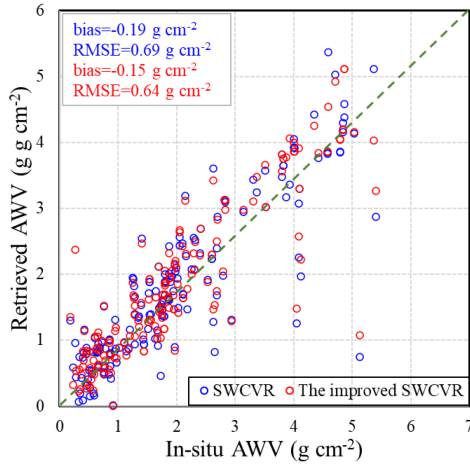
Fig. 10. Comparison between the in situ AWV and the retrieved AWV using the proposed method and SWCVR method.
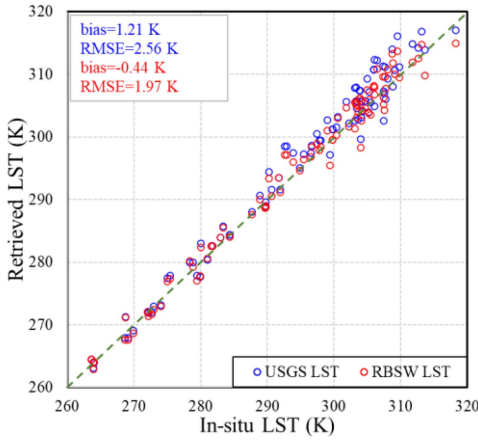

Fig. 11. Comparison between the in situ LST and the retrieved LST using the proposed method and RTE method (USGS).

with its size, which forms a paradox in the perspective of the performance of SWCVR. In the improved SWCVR method, this paradox can be effectively alleviated by grouping pixels based on LSE. As shown in Fig. 8, the RMSE between retrieved and MODIS AWVs decreases with the window size when the window size is below 80, and the RMSE decrease with the group number when the window size is above 40. The atmosphere is more spatially homogeneous than the land surface. In this article, the window size was set to 100 (corresponding to a spatial resolution of 3 km), and the group number was set to 3. Compared with MODIS AWV, the AWV retrieved using improved SWCVR has a bias of -0.27 g cm^{-2} and RMSE of 0.40 g cm^{-2}. Validation using in situ AWV data from AERONET stations shows that the total bias (RMSE) of the improved SWCVR is -0.19 g cm^{-2} (0.69 g cm^{-2}).

B. LST Retrieval From Landsat 9 TIR-2 Data

The simulation data were divided two parts, including two thirds of simulation data for fitting the RBSW algorithm and another one third for validating RBSW algorithm. The total

RMSE of LST retrieval using the independent validating simulation data set is 0.51 K, which is close to the RMSE in the fitting process (0.46 K). This indicates that the RBSW algorithm has a good accuracy and is generally applicable. In addition, the sensitivity of RBSW algorithm was analyzed considering different land surface and atmosphere conditions. Within the usual error range of input parameters, the overall LST error using RBSW algorithm is less than 1.75 K. The cross validation with USGS LST showed that the bias and RMSE between the estimated LST and USGS LST are -1.97 and 2.12 K, respectively. This LST difference is mainly caused by the different LST retrieval algorithms. The proposed method is two channels SW method, whereas the USGS LST used a single channel RTE method [23].

The in situ LST data from HiWATER and SURFRAD sites were used to validate the retrieved LST from Landsat 9 TIRS-2 data. The bias (RMSE) of USGS LST at SURFRAD sites is 0.99 K (2.40 K), which is in good agreement with the results of Landsat 7 and 8 validated at same sites by Malakar et al. [23]. The retrieved LST from Landsat 9 using RBSW algorithm has a good accuracy, with a bias (RMSE) is 0.57 K (1.73 K) at SURFRAD sites, which is better than the LST accuracy of previous Landsat series sensors validated at same sites (i.e., Landsat 4/5/7/8) [62], [66]. This indicates that the SW algorithm has better performance in atmospheric correction compared with single channel algorithm considering that the same LSE estimation method is used.

V. CONCLUSION

This article developed a SW method for LST retrieval from the newly launched Landsat 9 TIRS-2 data. The AWV was calculated using the improved SWCVR method in which a method for grouping pixels was introduced to mitigate the impact of high spatial heterogeneity of LSE. The LSE was calculated by combining NDVI^{THM} and ASTER GED LSE data. The performance of the proposed method was evaluated using the simulation data and ground data.

The sensitivity analysis showed that the RBSW algorithm is more sensitive to the error in ε_{10} as compared to the error in ε_{11} and the same errors in both ε_{10} and ε_{11}. The RBSW algorithm is more sensitive to the at-sensor radiance error in a single channel than to the same error in L_{10} and L_{11}. The sensitivity of RBSW algorithm to the AWV decrease with LSE. When the uncertainties are 0.04 Wm^{-2}sr$^{-1}\mu$m^{-1} (i.e., NEΔT of 0.28 K at 300 K) for L_{10}, 0.01 for ε_{10}, 0.6 g cm^{-2} for AWV, the overall errors in LST are between 1.10 K and 1.74 K under different atmospheric and surface conditions.

The improved SWCVR method for estimating the AWV has a good accuracy, with a bias (RMSE) of -0.27 g cm^{-2} (0.40 g cm^{-2}), by cross validation with MODIS AWV data. Validation using in situ AWV data from AERONET stations shows that the total bias (RMSE) of the improved SWCVR is -0.19 g cm^{-2} (0.69 g cm^{-2}). The LST retrieval using the estimated AWV show a similar result to that using the MODIS AWV data. Therefore, the improved SWCVR method can provide an optional means to obtain AWV for LST retrieval from Landsat

9 TIRS-2 data, especial for the region with no overlap between MODIS and Landsat 9 data.

Validation result based on the simulation data showed that the RMSE of RBSW algorithm is less than 1 K under AWV of lower than 5.0 g cm^{-2} and less than 2.5 K under AWV of lower than 7.0 g cm^{-2}. The total bias and total RMSE of RBSW algorithm for whole AWV range are 0.06 and 0.51 K, respectively. In terms of the validation using SURFRAD and HiWATER in situ measurements, the proposed method has a bias of 0.44 K and RMSE of 1.98 K, respectively, showing a higher accuracy as compared to the USGS Landsat ARD LST product.

In summary, it is effective for the proposed method to retrieve LST from Landsat 9 TIRS-2 data. The main characteristic of the proposed method is that it does not depend on auxiliary atmospheric data, which can greatly improve its practicality. More efforts are expected to paid to validate the estimated AWV and LST using the proposed method with more land covers, wider spatial ranges and long time series.

ACKNOWLEDGMENT

REFERENCES

[1] T. Hu et al., "Monitoring agricultural drought in Australia using MTSAT-2 land surface temperature retrievals," *Remote Sens. Environ.*, vol. 236, 2020, Art. no. 111419.

[2] S. A. Sahaar, J. D. Niemann, and A. Elhaddad, "Using regional characteristics to improve uncalibrated estimation of rootzone soil moisture from optical/thermal remote-sensing," *Remote Sens. Environ.*, vol. 273, 2022, Art. no. 112982.

[3] Y. Bai, N. Bhattarai, K. Mallick, S. Zhang, T. Hu, and J. Zhang, "Thermally derived evapotranspiration from the surface temperature initiated closure (STIC) model improves cropland GPP estimates under dry conditions," *Remote Sens. Environ.*, vol. 271, 2022, Art. no. 112901.

[4] L. Olivera-Guerra, C. Mattar, O. Merlin, C. Durán-Alarcón, A. Santamaría-Artigas, and R. Fuster, "An operational method for the disaggregation of land surface temperature to estimate actual evapotranspiration in the arid region of Chile," *ISPRS J. Photogramm. Remote Sens.*, vol. 128, pp. 170–181, 2017.

[5] Q. Meng, L. Zhang, Z. Sun, F. Meng, L. Wang, and Y. Sun, "Characterizing spatial and temporal trends of surface urban heat island effect in an urban main built-up area: A 12-year case study in Beijing, China," *Remote Sens. Environ.*, vol. 204, pp. 826–837, 2018.

[6] K. Liu, H. Su, X. Li, W. Wang, L. Yang, and H. Liang, "Quantifying spatial–temporal pattern of urban heat island in Beijing: An improved assessment using land surface temperature (LST) time series observations from Landsat, MODIS, and Chinese new satellite GaoFen-1," *IEEE J. Sel. Topics Appl. Earth Observ. Remote Sens.*, vol. 9, no. 5, pp. 2028–2042, May 2016.

[7] Q. Weng, "Thermal infrared remote sensing for urban climate and environmental studies: Methods, applications, and trends," *ISPRS J. Photogramm. Remote Sens.*, vol. 64, no. 4, pp. 335–344, 2009.

[8] R. Wang et al., "Geographical detection of urban thermal environment based on the local climate zones: A case study in Wuhan, China," *Remote Sens.*, vol. 14, no. 5, 2022, Art. no. 1067.

[9] T. Hu et al., "Estimation of upward longwave radiation from vegetated surfaces considering thermal directionality," *IEEE Trans. Geosci. Remote Sens.*, vol. 54, no. 11, pp. 6644–6658, Nov. 2016.

[10] M. Wang et al., "Comparison of spatial interpolation and regression analysis models for an estimation of monthly near surface air temperature in China," *Remote Sens.*, vol. 9, no. 12, 2017, Art. no. 1278.

[11] T. Smith and B. Bookhagen, "Changes in seasonal snow water equivalent distribution in High Mountain Asia (1987 to 2009)," *Sci. Adv.*, vol. 4, no. 1, 2018, Art. no. e1701550.

[12] W. W. Immerzeel, L. P. Van Beek, and M. F. Bierkens, "Climate change will affect the Asian water towers," *Science*, vol. 328, no. 5984, pp. 1382–1385, 2010.

[13] B. Bond-Lamberty and A. Thomson, "Temperature-associated increases in the global soil respiration record," *Nature*, vol. 464, no. 7288, pp. 579–582, 2010.

[14] J. Hansen, R. Ruedy, M. Sato, and K. Lo, "Global surface temperature change," *Rev. Geophys.*, vol. 48, no. 4, 2010.

[15] Z. Zhang et al., "A review of satellite synthetic aperture radar interferometry applications in permafrost regions: Current status, challenges, and trends," *IEEE Geosci. Remote Sens. Mag.*, vol. 10, no. 3, pp. 93–114, Sep. 2022.

[16] J. Townshend et al., "The 1 km resolution global data set: Needs of the international geosphere biosphere programme," *Int. J. Remote Sens.*, vol. 15, no. 17, pp. 3417–3441, 1994.

[17] Z.-L. Li et al., "Satellite-derived land surface temperature: Current status and perspectives," *Remote Sens. Environ.*, vol. 131, pp. 14–37, 2013.

[18] T. Hu et al., "Continental-scale evaluation of three ECOSTRESS land surface temperature products over Europe and Africa: Temperature-based validation and cross-satellite comparison," *Remote Sens. Environ.*, vol. 282, 2022, Art. no. 113296.

[19] J. McCorkel et al., "Landsat 9 thermal infrared sensor 2 characterization plan overview," in *Proc. IEEE Int. Geosci. Remote Sens. Symp.*, 2018, pp. 8845–8848.

[20] M. Wang et al., "An efficient framework for producing Landsat-based land surface temperature data using Google Earth engine," *IEEE J. Sel. Topics Appl. Earth Observ. Remote Sens.*, vol. 13, pp. 4689–4701, Aug. 2020.

[21] M. Wang, Z. Zhang, T. Hu, and X. Liu, "A practical single-channel algorithm for land surface temperature retrieval: Application to Landsat series data," *J. Geophys. Res., Atmos.*, vol. 124, no. 1, pp. 299–316, 2019.

[22] F. Wang, Z. Qin, C. Song, L. Tu, A. Karnieli, and S. Zhao, "An improved mono-window algorithm for land surface temperature retrieval from Landsat 8 thermal infrared sensor data," *Remote Sens.*, vol. 7, no. 4, pp. 4268–4289, 2015.

[23] N. K. Malakar, G. C. Hulley, S. J. Hook, K. Laraby, M. Cook, and J. R. Schott, "An operational land surface temperature product for Landsat thermal data: Methodology and validation," *IEEE Trans. Geosci. Remote Sens.*, vol. 56, no. 10, pp. 5717–5735, Oct. 2018.

[24] S.-B. Duan et al., "Land-surface temperature retrieval from Landsat 8 single-channel thermal infrared data in combination with NCEP reanalysis data and ASTER GED product," *Int. J. Remote Sens.*, vol. 40, no. 5-6, pp. 1763–1778, 2019.

[25] J. C. Jimenez-Munoz, J. A. Sobrino, D. Skokovic, C. Mattar, and J. Cristobal, "Land surface temperature retrieval methods from Landsat-8 thermal infrared sensor data," *IEEE Geosci. Remote Sens. Lett.*, vol. 11, no. 10, pp. 1840–1843, Oct. 2014.

[26] R. Niclòs et al., "Evaluation of Landsat-8 TIRS data recalibrations and land surface temperature split-window algorithms over a homogeneous crop area with different phenological land covers," *ISPRS J. Photogramm. Remote Sens.*, vol. 174, pp. 237–253, 2021.

[27] Q. Vanhellemont, "Combined land surface emissivity and temperature estimation from Landsat 8 OLI and TIRS," *ISPRS J. Photogramm. Remote Sens.*, vol. 166, pp. 390–402, 2020.

[28] A. Gerace, T. Kleynhans, R. Eon, and M. Montanaro, "Towards an operational, split window-derived surface temperature product for the thermal infrared sensors onboard Landsat 8 and 9," *Remote Sens.*, vol. 12, no. 2, pp. 1–15, 2020.

[29] J. G. Masek et al., "Landsat 9: Empowering open science and applications through continuity," *Remote Sens. Environ.*, vol. 248, 2020, Art. no. 111968.

[30] L. M. McMillin, "Estimation of sea surface temperatures from two infrared window measurements with different absorption," *J. Geophys. Res.*, vol. 80, no. 36, pp. 5113–5117, 1975.

[31] J. C. Price, "Land surface temperature measurements from the split window channels of the NOAA 7 Advanced very high resolution radiometer," *J. Geophys. Res., Atmos.*, vol. 89, no. D5, pp. 7231–7237, 1984.

[32] F. Becker and Z.-L. Li, "Towards a local split window method over land surfaces," *Remote Sens.*, vol. 11, no. 3, pp. 369–393, 1990.

[33] G. Franc and A. Cracknell, "Retrieval of land and sea surface temperature using NOAA-11 AVHRR· data in north-eastern Brazil," *Int. J. Remote Sens.*, vol. 15, no. 8, pp. 1695–1712, 1994.

[34] J.-C. Jiménez-Muñoz and J. Sobrino, "Split-window coefficients for land surface temperature retrieval from low-resolution thermal infrared sensors," *IEEE Geosci. Remote Sens. Lett.*, vol. 5, no. 4, pp. 806–809, Oct. 2008.

[35] Z. Qin, G. Dall'Olmo, A. Karnieli, and P. Berliner, "Derivation of split window algorithm and its sensitivity analysis for retrieving land surface temperature from NOAA-advanced very high resolution radiometer data," *J. Geophys. Res., Atmos.*, vol. 106, no. D19, pp. 22655–22670, 2001.

[36] O. Rozenstein, Z. Qin, Y. Derimian, and A. Karnieli, "Derivation of land surface temperature for Landsat-8 TIRS using a split window algorithm," *Sensors*, vol. 14, no. 4, pp. 5768–5780, 2014.

[37] H. Ren, X. Ye, R. Liu, J. Dong, and Q. Qin, "Improving land surface temperature and emissivity retrieval from the Chinese Gaofen-5 satellite using a hybrid algorithm," *IEEE Trans. Geosci. Remote Sens.*, vol. 56, no. 2, pp. 1080–1090, Feb. 2018.

[38] J. Sobrino and N. Raissouni, "Toward remote sensing methods for land cover dynamic monitoring: Application to Morocco," *Int. J. Remote Sens.*, vol. 21, no. 2, pp. 353–366, 2000.

[39] D. Sun and R. T. Pinker, "Estimation of land surface temperature from a Geostationary Operational environmental Satellite (GOES-8)," *J. Geophys. Res., Atmos.*, vol. 108, no. D11, pp. 6_1–6_1, 2003.

[40] Z. Wan, "New refinements and validation of the collection-6 MODIS land-surface temperature/emissivity product," *Remote Sens. Environ.*, vol. 140, pp. 36–45, 2014.

[41] J. Guo, H. Ren, Y. Zheng, S. Lu, and J. Dong, "Evaluation of land surface temperature retrieval from Landsat 8/TIRS images before and after stray light correction using the SURFRAD dataset," *Remote Sens.*, vol. 12, no. 6, 2020, Art. no. 1023.

[42] Z. Wan and J. Dozier, "A generalized split-window algorithm for retrieving land-surface temperature from space," *IEEE Trans. Geosci. Remote Sens.*, vol. 34, no. 4, pp. 892–905, Jul. 1996.

[43] T. Hu et al., "Influence of emissivity angular variation on land surface temperature retrieved using the generalized split-window algorithm," *Int. J. Appl. Earth Observ. Geoinf.*, vol. 82, 2019, Art. no. 101917.

[44] X. Ye, H. Ren, R. Liu, Q. Qin, Y. Liu, and J. Dong, "Land surface temperature estimate from chinese Gaofen-5 Satellite data using split-window algorithm," *IEEE Trans. Geosci. Remote Sens.*, vol. 55, no. 10, pp. 5877–5888, Oct. 2017.

[45] D. Sun and R. Pinker, "Retrieval of surface temperature from the MSG-SEVIRI observations: Part I. Methodology," *Int. J. Remote Sens.*, vol. 28, no. 23, pp. 5255–5272, 2007.

[46] M. Wang et al., "A radiance-based split-window algorithm for land surface temperature retrieval: Theory and application to MODIS data," *Int. J. Appl. Earth Observ. Geoinf.*, vol. 76, pp. 204–217, 2019.

[47] H. Ren et al., "Atmospheric water vapor retrieval from Landsat 8 thermal infrared images," *J. Geophys. Res., Atmos.*, vol. 120, no. 5, pp. 1723–1738, 2015.

[48] Z.-L. Li, L. Jia, Z. Su, Z. Wan, and R. Zhang, "A new approach for retrieving precipitable water from ATSR2 split-window channel data over land area," *Int. J. Remote Sens.*, vol. 24, no. 24, pp. 5095–5117, 2003.

[49] J. A. Sobrino, Z.-L. Li, M. P. Stoll, and F. Becker, "Improvements in the split-window technique for land surface temperature determination," *IEEE Trans. Geosci. Remote Sens.*, vol. 32, no. 2, pp. 243–253, Mar. 1994.

[50] S. Zhou and J. Cheng, "A framework for estimating clear-sky atmospheric total precipitable water (TPW) from VIIRS/S-NPP," *Remote Sens.*, vol. 11, no. 8, pp. 1–19, 2019.

[51] J. A. Sobrino et al., "Land surface emissivity retrieval from different VNIR and TIR sensors," *IEEE Trans. Geosci. Remote Sens.*, vol. 46, no. 2, pp. 316–327, Feb. 2008.

[52] X. Meng et al., "Estimating land surface emissivity from ASTER GED products," *Remote Sens*, vol. 4619, pp. 382–396, 2016.

[53] G. C. Hulley, S. J. Hook, E. Abbott, N. Malakar, T. Islam, and M. Abrams, "The ASTER Global emissivity dataset (ASTER GED): Mapping earth's emissivity at 100 meter spatial scale," *Geophys. Res. Lett.*, vol. 42, no. 19, pp. 7966–7976, 2015.

[54] T. N. Carlson and D. A. Ripley, "On the relation between NDVI, fractional vegetation cover, and leaf area index," *Remote Sens. Environ.*, vol. 62, no. 3, pp. 241–252, 1997.

[55] S. L. Ermida, P. Soares, V. Mantas, F.-M. Göttsche, and I. F. Trigo, "Google Earth engine open-source code for land surface temperature estimation from the Landsat series," *Remote Sens.*, vol. 12, no. 9, 2020, Art. no. 1471.

[56] R. N. Halthore, T. F. Eck, B. N. Holben, and B. L. Markham, "Sun photometric measurements of atmospheric water vapor column abundance in the 940-nm band," *J. Geophys. Res., Atmos.*, vol. 102, no. D4, pp. 4343–4352, 1997.

[57] C. Ichoku et al., "Analysis of the performance characteristics of the five-channel Microtops II sun photometer for measuring aerosol optical thickness and precipitable water vapor," *J. Geophys. Res., Atmos.*, vol. 107, no. D13, pp. AAC 5–1–AAC 5–17, 2002.

[58] J. A. Augustine, J. J. DeLuisi, and C. N. Long, "SURFRAD-A national surface radiation budget network for atmospheric research," *Bull. Amer. Meteorol. Soc.*, vol. 81, no. 10, pp. 2341–2357, 2000.

[59] X. Yu, X. Guo, and Z. Wu, "Land surface temperature retrieval from Landsat 8 TIRS—Comparison between radiative transfer equation-based method, split window algorithm and single channel method," *Remote Sens.*, vol. 6, no. 10, pp. 9829–9852, 2014.

[60] S. Liu et al., "The Heihe Integrated Observatory Network: A basin-scale land surface processes observatory in China," *Vadose Zone J.*, vol. 17, no. 1, pp. 1–21, 2018.

[61] S. M. Liu et al., "A comparison of eddy-covariance and large aperture scintillometer measurements with respect to the energy balance closure problem," *Hydrol. Earth Syst. Sci.*, vol. 15, no. 4, pp. 1291–1306, 2011.

[62] S.-B. Duan et al., "Validation of Landsat land surface temperature product in the conterminous United States using in situ measurements from SURFRAD, ARM, and NDBC sites," *Int. J. Digit. Earth*, vol. 14, no. 5, pp. 640–660, 2021.

[63] J. Cheng, S. Liang, Y. Yao, and X. Zhang, "Estimating the optimal broadband emissivity spectral range for calculating surface longwave net radiation," *IEEE Geosci. Remote Sens. Lett.*, vol. 10, no. 2, pp. 401–405, Mar. 2013.

[64] Z. Zhang and G. He, "Generation of Landsat surface temperature product for China, 2000–2010," *Int. J. Remote Sens.*, vol. 34, no. 20, pp. 7369–7375, 2013.

[65] Z. Zhang et al., "Towards an operational method for land surface temperature retrieval from Landsat 8 data," *Remote Sens. Lett.*, vol. 7, no. 3, pp. 279–288, 2016.

[66] K. Li, K. Guan, C. Jiang, S. Wang, B. Peng, and Y. Cai, "Evaluation of four new land surface temperature (LST) products in the US corn belt: ECOSTRESS, GOES-R, Landsat, and Sentinel-3," *IEEE J. Sel. Topics Appl. Earth Observ. Remote Sens.*, vol. 14, pp. 9931–9945, Sep. 2021.

Mengmeng Wang received the B.Sc. degree in geographic information system from the HeFei University of Technology, Hefei, China, in 2012, and the Ph.D. degree in cartography and geographic information system from the Institute of Remote Sensing and Digital Earth, Chinese Academy of Sciences, Beijing, China, in 2017.

He is currently an Associate Professor with the School of Geography and Information Engineering, China University of Geosciences (Wuhan), Wuhan, China. His main research interests include thermal infrared quantitative remote sensing and their applications on nature hazards and agriculture.

Miao Li received the B.S. degree in remote sensing science and technology from Hebei University of Engineering, Handan, China, in 2020. She is currently working toward the M.S. degree in photogrammetry and remote sensing with the School of Geography and Information Engineering, China University of Geosciences, Wuhan, China.

Her major research interests include atmospheric remote sensing and hydrometeorological data science.

Zhengjia Zhang received the B.Sc. degree in geographic information system from HeFei University of Technology, Hefei, China, in 2012, and the Ph.D. degree in cartography and geographic information system from Institute of Remote Sensing and Digital Earth, Chinese Academy of Sciences, Beijing, China, in 2017.

He is currently an Associate Professor with the School of Geography and Information Engineering, the China University of Geosciences (Wuhan), Wuhan, China. His main research interests include synthetic aperture radar (SAR) interferometric technique, time-series interferometric SAR, and their applications on nature hazards and permafrost regions.

Guizhou Wang received the B.S. degree in surveying and mapping engineering from Jilin University, Changchun, China, in 2008, and the M.S. degree in cartography and geographic information systems and the Ph.D. degree in signal and information processing from the University of Chinese Academy of Sciences (CAS), Beijing, China, in 2011 and 2014, respectively.

He is a Senior Engineer with the Aerospace Information Research Institute, CAS. His research interests include intelligent processing of high spatial resolution remote sensing images, such as image segmentation and classification.

Tian Hu received the B.E. degree in remote sensing science and technology from Wuhan University, Wuhan, China, in 2013, and the Ph.D. degrees in cartography and geoinformation system from the University of Chinese Academy of Sciences, Beijing, China, in 2018 and in environmental science from Griffith University, Brisbane, QLD, Australia, in 2020.

He is currently a Research Scientist with Luxembourg Institute of Science and Technology, Luxembourg, U.K. His research interests include thermal remote sensing of surface properties, thermal directionality, surface energy balance modeling, ecohydrology, and ecosystem functioning.

Hua Li received the B.Sc. degree in geographic information system from Xi'an University of Science and Technology, Xi'an, China, in 2004, the M.Sc. degree in cartography and geographic information system from Central South University, Changsha, China, in 2007, and the Ph.D. degree in cartography and geographic information system from the Institute of Remote Sensing Applications, Chinese Academy of Science, Beijing, China, in 2010.

He is currently an Associate Researcher with the State Key Laboratory of Remote Sensing Science, Aerospace Information Research Institute, Chinese Academy of Science. His research interests include retrieving and validating land surface temperature/emissivity from satellite data.

Guojin He received the B.Sc. degree in geology from Fuzhou University Fuzhou, China, in 1989, the M.Sc. degree in remote sensing of geology from the China University of Geosciences, Wuhan, China, in 1992, and the Ph.D. degree in geology from the Institute of Geology, Chinese Academy of Sciences (CAS), Beijing, China, in 1998.

He is currently a Professor with the Aerospace Information Research Institute, CAS. His research interests include big remote sensing data intelligence as well as using information retrieved from satellite remote sensing images, in combination with other sources of data to support better understanding of the Earth.

Junlei Tan received the B.Sc. degree in geographic information system from Hebei Normal University, Shijiazhuang, China, in 2007, the M.S. degree in cartography and geographic information system from Cold and Arid Regions Environmental and Engineering Research Institute, Chinese Academy of Sciences, Lanzhou, China, in 2010, and the Ph.D. degree in cartography and geographic information system from the Northwest Institute of Eco-Environment and Resources, Chinese Academy of Sciences, Lanzhou, China, in 2021.

He is currently an Engineer with the Key Laboratory of Remote Sensing of Gansu Province and the Heihe Remote Sensing Experimental Research Station, Northwest Institute of Eco-Environment and Resources, Chinese Academy of Sciences. His research interests include satellite land surface temperature/emissivity validation, remote sensing data application and reconstruction.

Zhaoming Zhang received the B.Sc. degree in geographic information system from Henan University, Kaifeng, China, in 2003, the M.Sc. degree in satellite image processing in 2006 from China Remote Sensing Satellite Ground Station, Chinese Academy of Sciences (CAS), Beijing, China, where he received the Ph.D. degree in cartography and geographic information system from the Institute of Remote Sensing Applications in 2009.

He is currently a Professor with the Aerospace Information Research Institute, CAS. His research interests include information extraction from satellite image and remote sensing applications.

Xiuguo Liu received the B.E. and M.E. degrees in computer and application and the Ph.D. degree in cartography and geographic information engineering from the China University of Geosciences (CUG), Wuhan, China, in 1991, 1999, and 2004, respectively.

He is currently a Professor with the School of Geography and Information Engineering, CUG. His research interests include polarimetric SAR, interferometric SAR theories, geographic information utilization, and three-dimensional geological modeling.